

# High-Mobility Multilayered MoS<sub>2</sub> Flakes with Low Contact Resistance Grown by Chemical Vapor Deposition

Jingying Zheng, Xingxu Yan, Zhixing Lu, Hailong Qiu, Guanchen Xu, Xu Zhou, Peng Wang, Xiaoqing Pan, Kaihui Liu, and Liying Jiao\*

Atomically 2D MoS<sub>2</sub> with intrinsic band gap has attracted tremendous attentions due to its significant potential for novel electronic and optoelectronic devices.<sup>[1]</sup> However, the relatively low mobility (even lower than polycrystalline silicon) of this material greatly hinders its practical applications.<sup>[2,3]</sup> Intensive studies have been focused on optimizing the synthesis and pushing the electrical performance of monolayer (1L) MoS<sub>2</sub>.<sup>[4–6]</sup> By contrast, relevant research on multilayer (ML) MoS<sub>2</sub> is quite rare. Actually, multilayered MoS<sub>2</sub> exhibits much higher mobility and drive currents than 1L MoS<sub>2</sub> due to the higher density of states<sup>[7–9]</sup> and consequentially is more attractive for applications in thin film transistors,<sup>[9]</sup> logic devices,<sup>[10]</sup> and sensors.<sup>[11]</sup> However, the excellent performances of ML MoS<sub>2</sub> reported so far are obtained from mechanically exfoliated MoS<sub>2</sub> which is not suitable for practical applications and only polycrystalline ML MoS<sub>2</sub> films have been synthesized by chemical vapor deposition (CVD) showing much lower mobility of 0.01–13 cm<sup>2</sup> V<sup>-1</sup> s<sup>-1</sup>.<sup>[12–16]</sup> Therefore, a controllable synthesis approach for producing highly crystalline ML MoS<sub>2</sub> flakes is highly desired. Besides the controllable synthesis of high-quality ML MoS<sub>2</sub>, contact engineering for ML MoS<sub>2</sub> is

also critical for improving their field-effect mobility as the contact resistance for ML MoS<sub>2</sub> is mainly contributed by the large interlayer resistance resulted from the indirect contact between the lower layers and electrodes.<sup>[7,8,17–19]</sup> Obviously, exposing the edges of each MoS<sub>2</sub> layer prior to the deposition of electrodes is the most effective way to ensure the sufficient contacts for the lower layers to the electrodes and thus reduce whole contact resistance by subtracting the interlayer resistance in ML MoS<sub>2</sub>, but so far, this strategy has not been realized experimentally.

To advance the practical applications of ML MoS<sub>2</sub>, we addressed the both challenges discussed above at the same time by developing a CVD approach for growing highly crystalline ML MoS<sub>2</sub> flakes with gradually shrinking basal planes from the bottom to the top layers. Up to 20 layers (L) of MoS<sub>2</sub> are stacked in a well-defined AA order and terminated with atomically smooth Mo zigzag (zz)-edges in each layer. The multilayer channels, together with atomically ordered edges and the ideal contact geometry make these CVD-grown ML MoS<sub>2</sub> flakes exhibit superior electrical performance than exfoliated ML MoS<sub>2</sub>. Moreover, besides field effect transistors, these ML MoS<sub>2</sub> flakes are also suitable for building rectifying diodes based on the 1L-ML MoS<sub>2</sub> junctions. Our approach makes high-quality ML MoS<sub>2</sub> easily accessible for building high-performance electronic devices with versatile functionalities and thus makes 2D MoS<sub>2</sub> more competitive for future electronics.

Our synthesis strategy is based on the layer-by-layer growth of MoS<sub>2</sub> by the rapid sulfurization of Mo oxides in gas phase in a confined space as illustrated in **Figure 1a**. To achieve the suitable growth atmosphere, we utilize the electrochemically oxidized Mo foil as growth precursor, which is composed of Mo oxides with varied oxidation states (from IV to VI) and thus enables the rapid and continuous feeding of Mo source in the gas phase (see more discussions in Figures S2 and S3, Supporting Information). To further increase the concentration of reactants, the growth of MoS<sub>2</sub> is performed in a confined space formed by covering the growth substrate with a bended oxidized Mo foil. The thickness of the obtained flakes can be tuned from 1L to >20L by simply manipulating electrochemical anodization conditions to yield MoO<sub>x</sub> precursors with varied oxidation degree (Figure 1c–f and see more details in Figure S4, Supporting Information). By optimizing oxidation and growth parameters, thick MoS<sub>2</sub> flakes with 15–20L at a yield of ≈70% have been successfully obtained (Figure 1b). The sequentially decreased growth time from the bottom to the top layers naturally resulted in the ML flakes stacked by multiple concentric triangles with shrinking size as revealed by both optical microscopy and atomic force microscopy (AFM) imaging (Figure 1g,h). The length of the bottom layer for the obtained

J. Zheng, Z. Lu, Dr. H. Qiu, Dr. G. Xu, Prof. L. Jiao  
Key Laboratory of Organic Optoelectronics and  
Molecular Engineering of the Ministry of Education  
Department of Chemistry  
Tsinghua University  
Beijing 100084, China  
E-mail: ljiao@mail.tsinghua.edu.cn



Dr. X. Yan, Prof. P. Wang, Prof. X. Pan  
National Laboratory of Solid State Microstructures  
College of Engineering and Applied Sciences and  
Collaborative Innovation Center of Advanced Microstructures  
Nanjing University  
Nanjing 210093, China

X. Zhou, Prof. K. Liu  
State Key Laboratory for Mesoscopic Physics  
Collaborative Innovation Center of Quantum Matter  
School of Physics  
Center for Nanochemistry  
Peking University  
Beijing 100871, China

Prof. X. Pan  
Department of Chemical Engineering and Materials Science  
University of California–Irvine  
Irvine, CA 92697, USA

Prof. X. Pan  
Department of Physics and Astronomy  
University of California–Irvine  
Irvine, CA 92697, USA

DOI: 10.1002/adma.201604540

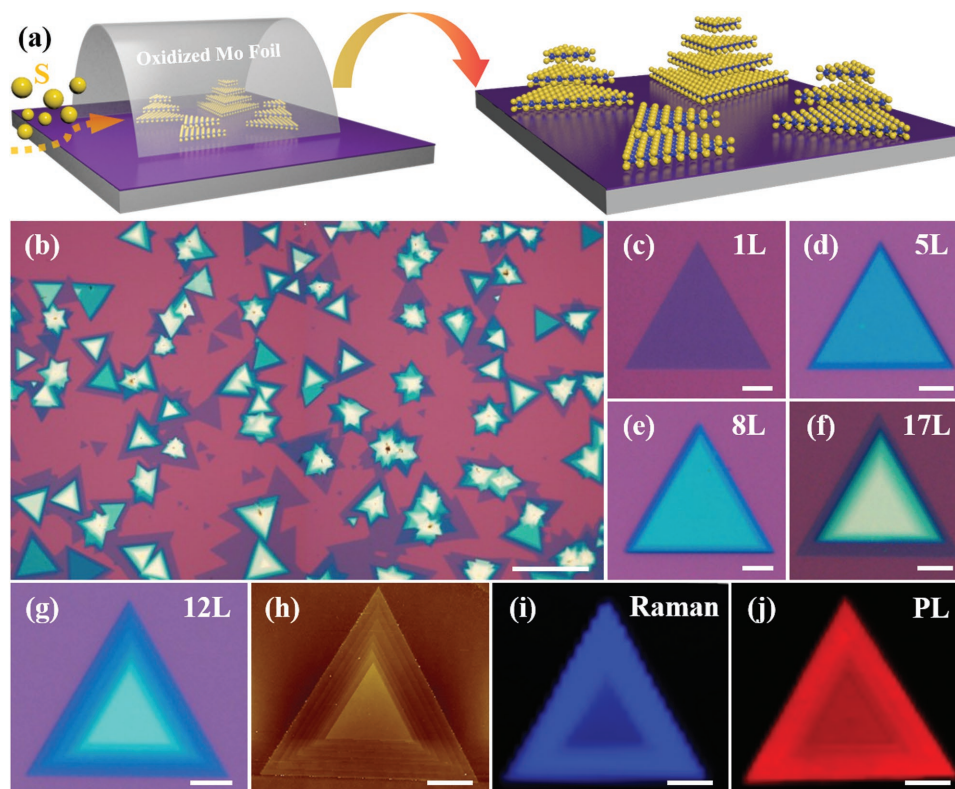


**Figure 1.** Synthesis of MoS<sub>2</sub> flakes with varied layer numbers. a) Schematics for the CVD growth of MoS<sub>2</sub> using arched oxidized Mo foil as precursor. b) Large scale optical image of the growth products, showing the growth of 15–20L MoS<sub>2</sub> at a yield of ≈70%. Scale bar: 50 μm. c–f) Optical images of CVD-grown MoS<sub>2</sub> flakes of 1, 5, 8, and 17L, respectively. g, h) Optical and AFM images of a 12L MoS<sub>2</sub> with ≈20 μm side length. i) Raman mapping image of the flake shown in (g) with 404 cm<sup>-1</sup> peak intensity. j) PL mapping image of the same flake with 1.80 eV peak intensity. Scale bars in (c–j): 5 μm.

MoS<sub>2</sub> flakes was mostly in the range of ≈20–30 μm and can be up to ≈50 μm, which is suitable for making field-effect devices with varied channel lengths up to tens of micrometers.

Both theoretical and experimental studies on mechanically exfoliated MoS<sub>2</sub> have revealed that the band structure and properties of MoS<sub>2</sub> are highly depended on the number of layers.<sup>[20–23]</sup> However, the effects of layer numbers on highly crystalline CVD-grown MoS<sub>2</sub> have not been explored due to the lack of such samples. We investigated the layer-dependent properties of CVD-grown MoS<sub>2</sub> flakes in details with Raman, photoluminescence (PL), and optical second-harmonic generation (SHG) spectroscopy. The number of layers of the CVD-grown flakes was determined by careful AFM measurements (Figure S5, Supporting Information). Raman spectra of as-grown MoS<sub>2</sub> flakes with thickness of 1–10L demonstrated that the peak position difference between A<sub>1g</sub> and E<sup>1</sup><sub>2g</sub> modes increased gradually with increasing layer numbers and converged to the bulk values for flakes of 6L or more, showing exactly the same trend as in the mechanically exfoliated ML MoS<sub>2</sub> (Figure 2a,b,e).<sup>[20,21]</sup> In addition, similar to exfoliated MoS<sub>2</sub>, the Raman peak intensities first increased and then decreased with the number of layers showing the maximized intensity at 4L, but the full width at half maximum (FWHM) of both Raman modes were independent on layer numbers (Figure S6, Supporting Information). These spectroscopic features elucidated that the layers in CVD-grown ML flakes had comparable coupling as in mechanically exfoliated flakes.

Identical PL peak positions at ≈1.8 eV and similar intensity-layer numbers dependence for both CVD-grown and exfoliated ML MoS<sub>2</sub> suggested comparable optical quality and analogous changes of band structure with the number of layers (Figure 2c,f).<sup>[14,22]</sup> We also performed Raman and PL intensity mapping on the CVD-grown ML MoS<sub>2</sub> flakes and the mapping images matched well with the optical and AFM images of the same flakes (Figure 1i,j). And the step region exhibited stronger Raman and PL intensity with smaller frequency difference of two Raman modes than the center platform and clearly demonstrated the thickness-dependent peak positions and intensities (Figure S7, Supporting Information). Moreover, SHG spectra were utilized to investigate the symmetry and stacking configuration of MoS<sub>2</sub> flakes based on the obvious intensity difference between centrosymmetric and noncentrosymmetric structures.<sup>[23]</sup> In contrast to the extremely low SHG intensity for mechanically exfoliated ML MoS<sub>2</sub> with centrosymmetric AB stacking mode, the CVD-grown ML flakes showed strong SHG signal and the intensity was monotonically increasing with the layer numbers (Figure 2d,g). Additionally, the polarization-resolved SHG intensity of CVD-grown MoS<sub>2</sub> flakes with varied number of layers exhibited strong sixfold rotational symmetry with petals lying along the perpendicular bisectors of each flake (Figure S8, Supporting Information), which indicated that the CVD-grown MoS<sub>2</sub> flakes presented AA stacked configuration with symmetry-breaking nature, where the direction of in-plane Mo–S bonds was same in different layers.<sup>[24,25]</sup>

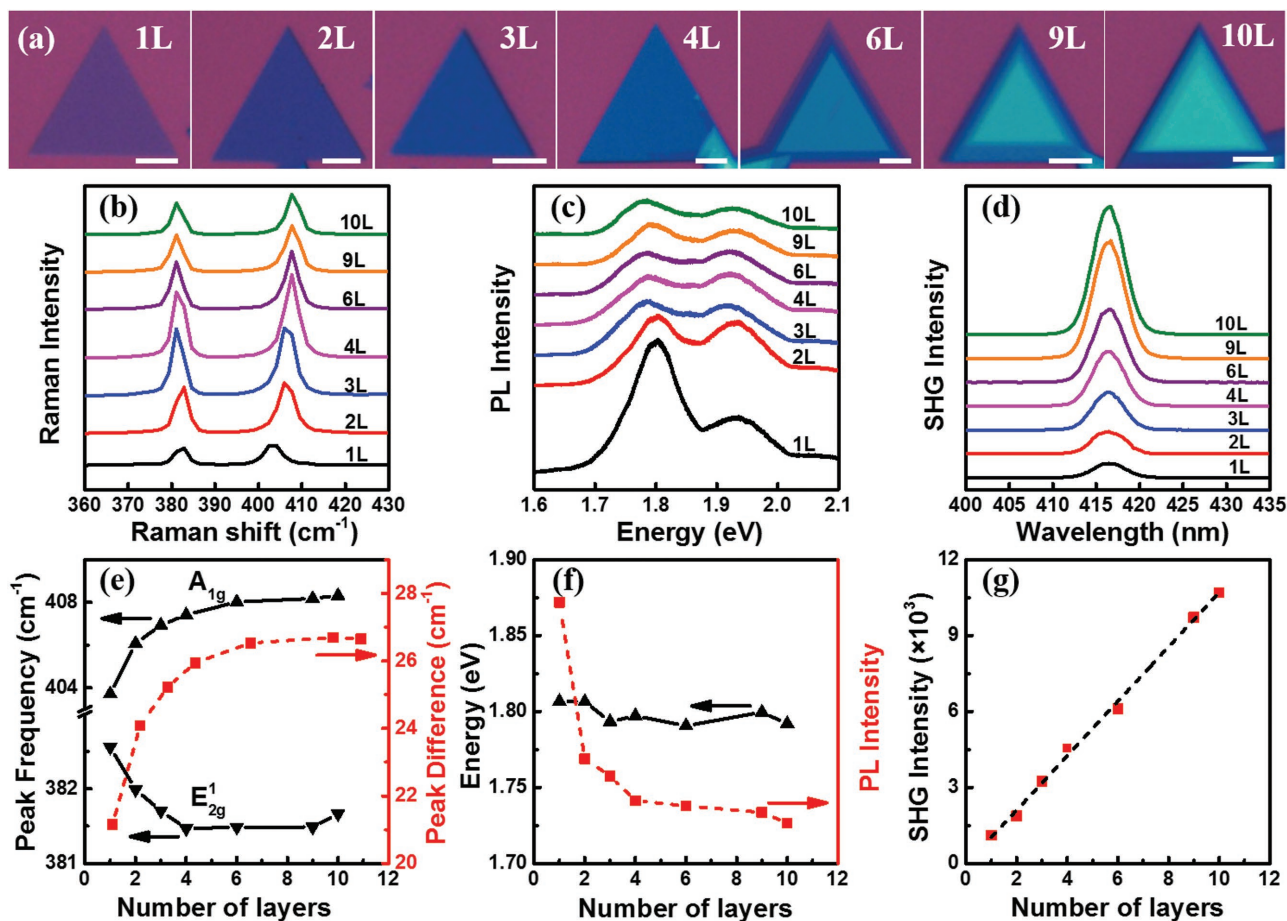


**Figure 2.** Layer-dependent spectroscopic characterizations of CVD-grown MoS<sub>2</sub> flakes. a) Optical images of MoS<sub>2</sub> flakes of 1, 2, 3, 4, 6, 9, and 10L, respectively. Scale bar: 5  $\mu\text{m}$ . b–d) Raman, PL, and SHG spectra of the MoS<sub>2</sub> flakes shown in (a). e) Layer-dependent frequencies of  $E_{2g}^1$ ,  $A_{1g}$  Raman mode and their difference. f) Layer-dependent PL peak position and intensities. g) SHG intensities as the function of layer numbers.

To further evaluate the crystallinity and determine edges structures and stacking configuration of the CVD-grown MoS<sub>2</sub> multilayers, we transferred the ML flakes to the holey carbon grids for transmission electron microscopy (TEM) and scanning transmission electron microscopy (STEM) characterizations. TEM images captured on ML MoS<sub>2</sub> flakes also displayed the unique concentric triangular geometry with exposed edges of  $\approx 200\text{--}600$  nm widths for each layer (Figure 3a), consistent with the AFM measurements. Selected-area electron diffraction (SAED) patterns taken at both 1L and ML regions exhibited only one set of hexagonally arranged diffraction spots, indicating the single crystalline nature of the flake over a large area and almost  $0^\circ$  twisted angle between different layers (Figure 3b,c, and Figure S9, Supporting Information). Moreover, STEM high-angle annular dark-field (HAADF) imaging with atomic resolution revealed that the edges of each layer were atomically smooth with Mo-terminated *zz* structures (Figure 3d and Figure S9, Supporting Information), which exhibited metallic states as elucidated by both theoretical calculations and scanning tunneling microscopy (STM) imaging<sup>[26–28]</sup> and therefore may enhance electron injection from MoS<sub>2</sub> to electrodes. To precisely identify stacking configuration in the CVD-grown MoS<sub>2</sub> samples, we compared the relative point intensity in

the captured STEM-HAADF images with those in the simulated images.<sup>[29]</sup> The experimental STEM-HAADF image of the bilayer MoS<sub>2</sub> region demonstrated nearly identical intensity profile to the simulated image with AA stacking order (Figure 3d,e and Figure S9, Supporting Information), where S atoms of one layer overlapped with the Mo atoms or the hexagonal centers of the adjacent layer as illustrated in Figure 3e and 3g, suggesting that these two layers were AA stacked.<sup>[30]</sup> In the similar way, AA stacked STEM images of 3–8L MoS<sub>2</sub> were also simulated (Figure 3f) and these simulated images also coincided well with experimentally captured images (Figure S9, Supporting Information). Combined STEM imaging with SHG measurements, we can confirm that the layers in the CVD-grown ML MoS<sub>2</sub> flakes maintained a well-defined AA stacked configuration. Owing to the broken inversion symmetry, such AA stacking order in obtained CVD-grown ML MoS<sub>2</sub> will be of great interest for symmetry-dependent properties of MoS<sub>2</sub>, including optical nonlinearity and valley polarization physics.<sup>[31]</sup>

As various microscopic and spectroscopic characterizations have confirmed that the obtained ML MoS<sub>2</sub> flakes are highly crystalline and the edges in each layer are exposed with atomically smooth Mo *zz*-structures, which are ideal for improving the mobility of ML MoS<sub>2</sub>, we further explored their electrical

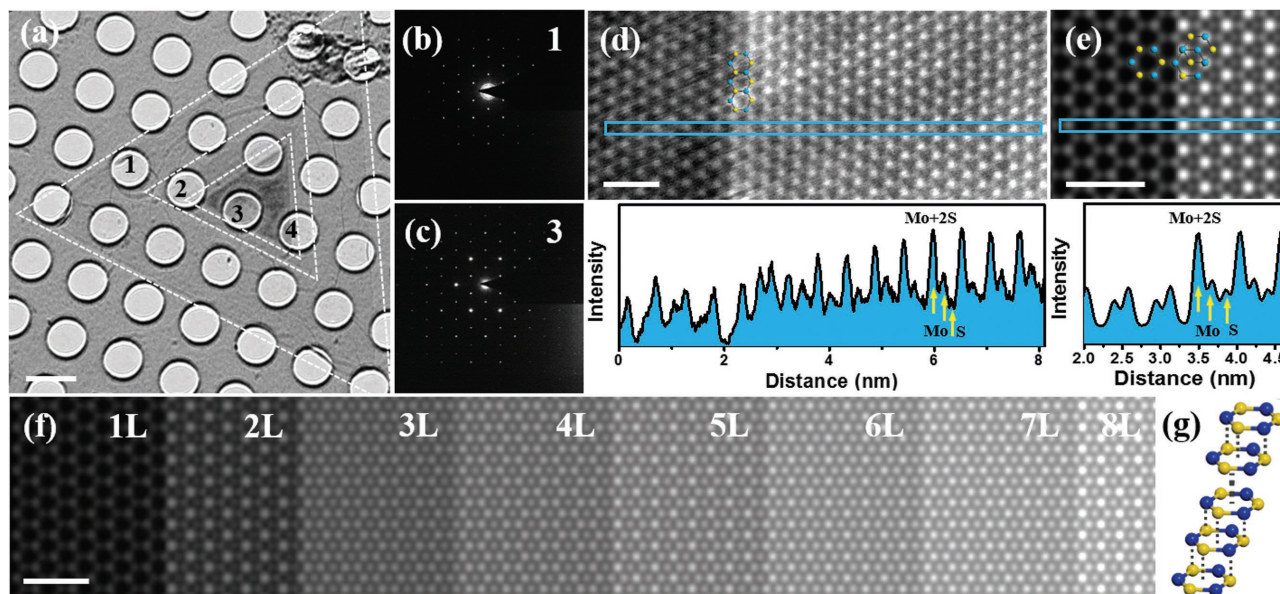


**Figure 3.** TEM and STEM characterizations of obtained multilayer MoS<sub>2</sub>. a) TEM image of CVD-grown ML MoS<sub>2</sub> flake suspended on a holey carbon TEM grid. Scale bar: 1 μm. SAED patterns taken at locations marked with b) 1 and c) 3 on the ML MoS<sub>2</sub> in (a). The SAED patterns of the locations marked with 2 and 4 are shown in Figure S7 (Supporting Information). d) STEM-HAADF image and e) simulated image at the 1–2L boundary of another ML MoS<sub>2</sub> flake shown in Figure S7 (Supporting Information). The blue and yellow ball presented Mo and S atom, respectively. Scale bar: 1 nm. f) Simulated STEM-HAADF image of 1–8L MoS<sub>2</sub> from left to right. Scale bar: 1 nm. g) Atomic configuration of AA stacked ML MoS<sub>2</sub>. The direction of in-plane Mo–S bonds was the same and S atoms of the top layer overlapped with the hexagonal centers of the bottom layer.

performance. Back-gated field-effect transistors (FETs) were fabricated by electron-beam lithography (EBL) and thermally evaporated 5/50 nm Ti/Au as source and drain electrodes on CVD-grown ML MoS<sub>2</sub> and also mechanically exfoliated samples for comparison. The typical transfer characteristics of the CVD-grown ML MoS<sub>2</sub> flake measured at room temperature in vacuum ( $\approx 10^{-5}$  mbar) behaved as an n-type semiconductor (Figure 4c). The estimated mobility of these ML device (>13L) can reach up to  $\approx 67$  cm<sup>2</sup> V<sup>-1</sup> s<sup>-1</sup> and the saturation current reached up to  $\approx 92$  μA μm<sup>-1</sup>, respectively, with on/off current ratios of  $\approx 10^6$ . We measured >30 CVD-grown MoS<sub>2</sub> (1–18L) FETs and observed that both their mobility and current increased with the increasing number of layers (<15L) (Figure 4e,f). Averaged mobility and current ( $V_{gs} = 40$  V,  $V_{ds} = 1$  V) for FETs fabricated on 10–18L CVD-grown MoS<sub>2</sub> were approximately four times and three times higher than those of 1L CVD-grown MoS<sub>2</sub> FETs (Figure S10, Supporting Information), respectively, due to the smaller bandgap,<sup>[19]</sup> higher carrier concentration,<sup>[9]</sup> and sufficient screening of the interfacial impurities in ML flakes.<sup>[8]</sup> For the exfoliated MoS<sub>2</sub> samples (Figure S11, Supporting Information), however, the mobility and current ( $V_{gs} = 40$  V,  $V_{ds} = 1$  V) showed nonmonotonic trend with the maximum of  $\approx 50$  cm<sup>2</sup> V<sup>-1</sup> s<sup>-1</sup> and 6 μA μm<sup>-1</sup> for 10–12L MoS<sub>2</sub>, respectively (Figure 4e,f). The decreased mobility and current in thicker mechanically exfoliated MoS<sub>2</sub> flakes are attributed to the increased interlayer resistance.<sup>[8,17]</sup> As the edges are abrupt in ML exfoliated flakes as illustrated in Figure 4a, the lower layers are covered by the top layers and therefore cannot directly contact with the electrodes. And consequently, electron needs to migrate across interlayers and thus introduces large interlayer resistance to the ML MoS<sub>2</sub> devices.<sup>[8,17]</sup> In contrast, the edges of each layer in CVD-grown ML MoS<sub>2</sub> flakes are

exposed to facilitate good contacts with electrodes (Figure 4b), assuring that the current can inject into the lower layers and thus reducing the contact resistance by minimizing the total interlayer resistance through the entire ML flake. Therefore, the field effect mobility and current of CVD-grown MoS<sub>2</sub> are superior to the exfoliated MoS<sub>2</sub>, especially for thicker MoS<sub>2</sub> (>13L). Furthermore, we etched away the terraced edges of as-grown ML flakes and made FETs on these etched flakes (Figure S12, Supporting Information). The averaged mobility of FETs made on 10–12L etched flakes with abrupt edges was  $\approx 15$  cm<sup>2</sup> V<sup>-1</sup> s<sup>-1</sup> and much lower than that of 10–12L as-grown flakes with terraced edges ( $\approx 55$  cm<sup>2</sup> V<sup>-1</sup> s<sup>-1</sup>), further confirming that the higher mobility of the CVD-grown ML MoS<sub>2</sub> flakes was attributed to their unique edge geometry. And this strategy can also be applied on continuous ML films for batch fabrication of high-performance MoS<sub>2</sub> FETs through a patterning-etching two-step process as we proposed in Figure S13 (Supporting Information). Besides their promising applications in FETs, these CVD-grown ML MoS<sub>2</sub> flakes are also suitable for constructing rectifying diodes simply utilizing the obvious differences in bandgap between 1L and ML regions on the same flake. The typical  $I_{ds}$ – $V_{ds}$  characteristics of the diode made on a 1–8L MoS<sub>2</sub> junction exhibited a forward/reverse current ratio of  $\approx 10^3$  measured at  $V_{gs} = 0$  V, demonstrating a simple and efficient approach for fabricating rectifying diodes based on homogeneous 2D junctions (Figure 4d).

In summary, we developed a controllable approach for producing high-quality ML MoS<sub>2</sub> and at the same time naturally introducing ideal contact geometry to these flakes for achieving the ultimate device performance based on 2D MoS<sub>2</sub>. The CVD-grown ML MoS<sub>2</sub> flakes present a well-defined AA stacking order with broken inversion symmetry which makes these ML MoS<sub>2</sub>

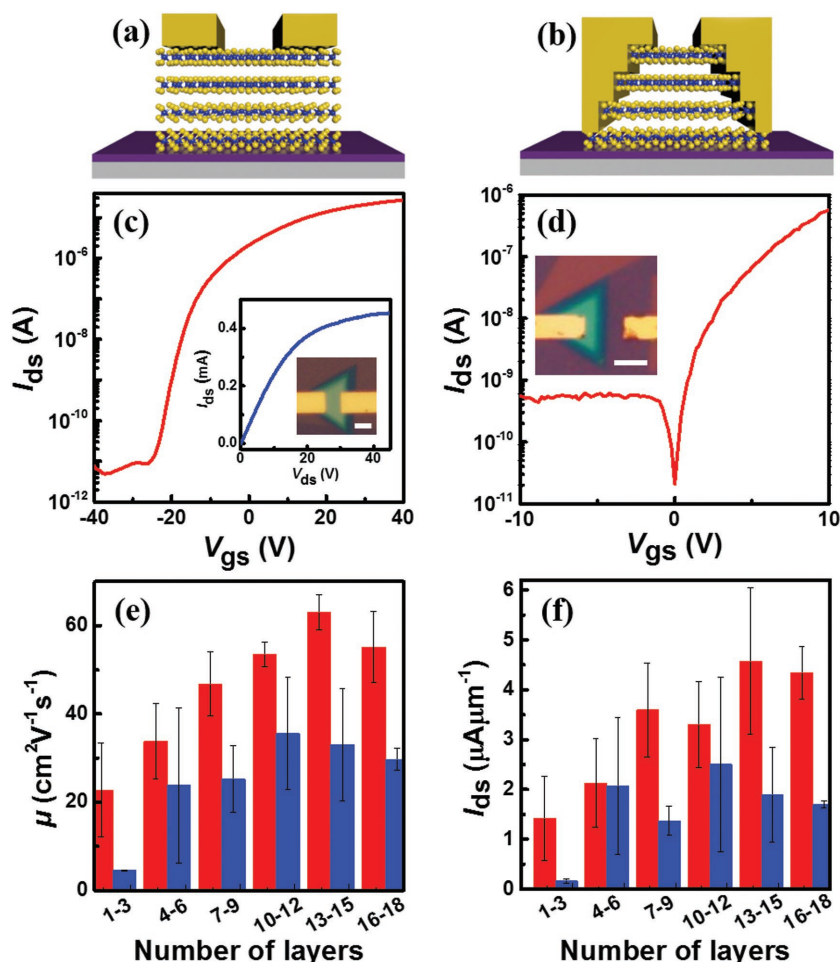


**Figure 4.** Electrical performances of the CVD-grown ML MoS<sub>2</sub> flakes. a, b) Schematic illustrations of the electrical contact geometries in ML exfoliated MoS<sub>2</sub> and CVD-grown MoS<sub>2</sub> flakes. c)  $I_{ds}$ – $V_{gs}$  characteristics of a 16L MoS<sub>2</sub> flake at the bias voltage of 1 V. Insets:  $I_{ds}$ – $V_{ds}$  curve at a gate voltage of 40 V and optical image of the device. Scale bar: 5  $\mu\text{m}$ . d)  $I_{ds}$ – $V_{gs}$  characteristics of 1–8L MoS<sub>2</sub> junction measured at a gate voltage of 0 V. Inset: Optical image of the device. Scale bar: 5  $\mu\text{m}$ . e) Statistics of electron mobility and f) current measured at  $V_{gs} = 40$  V and  $V_{ds} = 1$  V as the function of layer numbers in CVD-grown MoS<sub>2</sub> flakes (red columns) and mechanically exfoliated MoS<sub>2</sub> flakes (blue columns).

flakes hold great promise for addressing fundamental aspects on optical nonlinearity and valley physics. Layer-dependent Raman and PL spectra in these obtained MoS<sub>2</sub> exhibit similar trends to mechanically exfoliated MoS<sub>2</sub>, suggesting analogous interlayer interactions, band structure, and optical quality. The high crystallinity together with the unique geometry of CVD-grown ML MoS<sub>2</sub> flakes lead to quite high electron mobility for constructing both high-performance FETs and diodes. More importantly, the contact resistance is reduced in the CVD-grown ML MoS<sub>2</sub> flakes to a large extent as each layer can directly form conformal contacts to electrodes, and therefore, greatly enhances the electrical performance of 2D MoS<sub>2</sub> and makes this emerging material more competitive for future electronics. Moreover, our approach opens up a new avenue for the performance optimization of various 2D semiconductors by rational geometric design and controlled synthesis of these materials.

## Experimental Section

**Synthesis:** The growth precursor of MoO<sub>x</sub> was prepared by electrochemical anodization of Mo foils (Figure S1a, Supporting Information).<sup>[32]</sup> The anodization was carried out at voltages of 0.45–0.57 V for 30 min under a constant temperature of 30 °C. Afterward, the oxidized Mo foils were rinsed with water and then dried naturally. To synthesize MoS<sub>2</sub> flakes, Mo foil was arched and placed on a 300 nm SiO<sub>2</sub>/Si substrate and then loaded to the center of the furnace. Sulfur powder (Alfa-Aesar, 99.999%, 1.8 g) was placed at the upstream entry of the furnace (Figure S1b, Supporting Information). Next, the furnace was heated up to 700 °C at a rate of 20 °C min<sup>−1</sup> under the Ar flow at 100 sccm. After staying at 700 °C for 10 min, the temperature was increased to 850 °C and then held at 850 °C for 15 min. Then the temperature was increased to 900 °C and stayed for 30 min before the furnace naturally cooled down to room temperature. Sulfur powders were heated by an individual heating belt at ≈190 °C when the temperature of the furnace reached 630 °C and the heating was stopped when the furnace cooled to 400 °C.

**Characterizations:** Optical images were captured with Olympus BX 51M microscope. AFM images were taken with Bruker Dimension Icon in tapping mode. Raman and PL measurements were carried out with Horiba-Jobin-Yvon Raman system at 532 nm laser excitation with a power of 1 mW. Raman and PL mapping images were collected at the step of 0.7 and 0.4  $\mu\text{m}$ , respectively. The Si peak at 520.7 cm<sup>−1</sup> was used for calibration in the data analysis of Raman and PL spectra. SHG measurements were performed with a home-built setup. A femtosecond laser with 820 nm wavelength and 100 fs pulse duration was used as the excitation source at a repetition rate of 80 MHz. And the linearly polarized excitation light focused on the sample by a Nikon objective (N.A. = 0.9). TEM images and SAED patterns were acquired with F20 at 200 kV. STEM experiment was performed with the Titan 60–300, operating at 60 kV accelerating voltage. STEM-HAADF image simulations were calculated using a multislice based simulation software called QSTEM. All the input parameters, including probe size, convergence angle, and collection angles of the HAADF detector, were set according to the experimental conditions.<sup>[33]</sup> X-ray

photoelectron spectroscopy (XPS) was measured with Thermo Fisher ESCALAB 250Xi. The thermogravimetric analysis was carried out with NETZSCH STA 449F3 under argon flow at the heating rate of 5 °C min<sup>−1</sup>.

**Device Fabrication and Measurement:** EBL was used to define the markers on the growth substrate and then fabricate electrode patterns on selected MoS<sub>2</sub> flakes. Ti/Au (5/50 nm) films were thermally evaporated for contacts. The obtained FETs were measured with a probe station at room temperature under high vacuum ( $\approx 10^{-5}$  mbar) using Agilent B1500 A. The saturation current was normalized by the width. And the carrier mobility of FETs was estimated using the equation below:<sup>[34]</sup>

$$\mu = \frac{L}{W \times (\epsilon_0 \epsilon_r / d) \times V_{ds}} \times \frac{dI_{ds}}{dV_{gs}} \quad (1)$$

## Supporting Information

Supporting Information is available from the Wiley Online Library or from the author.

## Acknowledgements

L.J. acknowledges funding from the Natural Scientific Foundation of China (Grant Nos. 21322303, 51372134, and 21573125) and Tsinghua University Initiative Scientific Research Program. P.W. acknowledges funding from the National Natural Science Foundation of China (11474147), the National Basic Research Program of China (Grant No. 2015CB654900), and the Natural Science Foundation of Jiangsu Province (Grant No. BK20151383). K.L. acknowledges funding from the Natural Scientific Foundation of China (Grant No. 51522201) and the National Basic Research Program of China (Grant No. 2016YFA0300903).

Received: August 25, 2016

Revised: December 12, 2016

Published online:

- [1] Q. H. Wang, K. Kalantar-Zadeh, A. Kis, J. N. Coleman, M. S. Strano, *Nat. Nanotechnol.* **2012**, *7*, 699.
- [2] N. Petrone, J. Hone, D. Akinwande, *Nat. Commun.* **2015**, *5*, 1.
- [3] Y. Shi, H. Li, L.-J. Li, *Chem. Soc. Rev.* **2015**, *44*, 2744.
- [4] K. Kang, S. Xie, L. Huang, Y. Han, P. Y. Huang, K. F. Mak, C.-J. Kim, D. Muller, J. Park, *Nature* **2015**, *520*, 656.
- [5] G. H. Han, N. J. Kybert, C. H. Naylor, B. S. Lee, J. Ping, J. H. Park, J. Kang, S. Y. Lee, Y. H. Lee, R. Agarwal, A. T. C. Johnson, *Nat. Commun.* **2015**, *6*, 6128.
- [6] X. Wang, H. Feng, Y. Wu, L. Jiao, *J. Am. Chem. Soc.* **2013**, *135*, 5304.
- [7] S. Li, K. Wakabayashi, Y. Xu, S. Nakaharai, K. Komatsu, W.-W. Li, Y.-F. Lin, A. Aparecido-Ferreira, K. Tsukagoshi, *Nano Lett.* **2013**, *13*, 3546.
- [8] S. Das, H.-Y. Y. Chen, A. V. Penumatcha, J. Appenzeller, *Nano Lett.* **2012**, *13*, 100.
- [9] S. Kim, A. Konar, W.-S. Hwang, J. H. Lee, J. Lee, J. Yang, C. Jung, H. Kim, J.-B. Yoo, J.-Y. Choi, Y. W. Jin, S. Y. Lee, D. Jena, W. Choi, K. Kim, *Nat. Commun.* **2012**, *3*, 1011.
- [10] X. Liu, D. Qu, J. Ryu, F. Ahmed, Z. Yang, D. Lee, W. J. Yoo, *Adv. Mater.* **2016**, *28*, 2345.
- [11] H. Li, Z. Yin, Q. He, H. Li, X. Huang, G. Lu, D. W. H. Fam, A. I. Y. Tok, Q. Zhang, H. Zhang, *Small* **2012**, *8*, 63.
- [12] C. Ahn, J. Lee, H. U. Kim, H. Bark, M. Jeon, G. H. Ryu, Z. Lee, G. Y. Yeom, K. Kim, J. Jung, Y. Kim, C. Lee, T. Kim, *Adv. Mater.* **2015**, *27*, 5223.
- [13] Y.-C. Lin, W. Zhang, J.-K. Huang, K.-K. Liu, Y.-H. Lee, C.-T. Liang, C.-W. Chu, L.-J. Li, *Nanoscale* **2012**, *4*, 6637.
- [14] Y. Yu, C. Li, Y. Liu, L. Su, Y. Zhang, L. Cao, *Sci. Rep.* **2013**, *3*, 1866.
- [15] N. Choudhary, J. Park, J. Y. Hwang, W. Choi, *ACS Appl. Mater. Interfaces* **2014**, *6*, 21215.
- [16] K.-K. Liu, W. Zhang, Y.-H. Lee, Y.-C. Lin, M.-T. Chang, C.-Y. Su, C.-S. Chang, H. Li, Y. Shi, H. Zhang, C.-S. Lai, L.-J. Li, *Nano Lett.* **2012**, *2*, 1.
- [17] S. Das, J. Appenzeller, *Nano Lett.* **2013**, *13*, 3396.
- [18] Y. Xu, C. Cheng, S. Du, J. Yang, B. Yu, J. Luo, W. Yin, E. Li, S. Dong, P. Ye, X. Duan, *ACS Nano* **2016**, *10*, 4895.
- [19] A. Allain, J. Kang, K. Banerjee, A. Kis, *Nat. Mater.* **2015**, *14*, 1195.
- [20] C. Lee, H. Yan, L. E. Brus, T. F. Heinz, J. Hone, S. Ryu, *ACS Nano* **2010**, *4*, 2695.
- [21] H. Li, Q. Zhang, C. C. R. Yap, B. K. Tay, T. H. T. Edwin, A. Olivier, D. Baillargeat, *Adv. Funct. Mater.* **2012**, *22*, 1385.
- [22] A. Splendiani, L. Sun, Y. Zhang, T. Li, J. Kim, C. Y. Chim, G. Galli, F. Wang, *Nano Lett.* **2010**, *10*, 1271.
- [23] Y. Li, Y. Rao, K. F. Mak, Y. You, S. Wang, C. R. Dean, T. F. Heinz, *Nano Lett.* **2013**, *13*, 3329.
- [24] W. Hsu, Z. Zhao, L. Li, C. Chen, M. Chiu, P. Chang, *ACS Nano* **2014**, *8*, 1.
- [25] L. Zhang, K. Liu, A. B. Wong, J. Kim, X. Hong, C. Liu, T. Cao, S. G. Louie, F. Wang, P. Yang, *Nano Lett.* **2014**, *14*, 6418.
- [26] M. V. Bollinger, J. V. Lauritsen, K. W. Jacobsen, J. K. Nørskov, S. Helveg, F. Besenbacher, *Phys. Rev. Lett.* **2001**, *87*, 196803.
- [27] Y. Li, Z. Zhou, S. Zhang, Z. Chen, *J. Am. Chem. Soc.* **2008**, *130*, 16739.
- [28] X. Yin, Z. Ye, D. A. Chenet, Y. Ye, K. O. Brien, J. C. Hone, X. Zhang, *Science* **2014**, *344*, 488.
- [29] M. Xia, B. Li, K. Yin, G. Capellini, G. Niu, Y. Gong, W. Zhou, P. M. Ajayan, Y. H. Xie, *ACS Nano* **2015**, *9*, 12246.
- [30] K. Liu, L. Zhang, T. Cao, C. Jin, D. Qiu, Q. Zhou, A. Zettl, P. Yang, S. G. Louie, F. Wang, *Nat. Commun.* **2014**, *5*, 4966.
- [31] R. Suzuki, M. Sakano, Y. J. Zhang, R. Akashi, D. Morikawa, A. Harasawa, K. Yaji, K. Kuroda, K. Miyamoto, T. Okuda, K. Ishizaka, R. Arita, Y. Iwasa, *Nat. Nanotechnol.* **2014**, *9*, 611.
- [32] Y. Yang, H. Fei, G. Ruan, C. Xiang, J. M. Tour, *Adv. Mater.* **2014**, *26*, 8163.
- [33] C. T. Koch, *Determination of Core Structure Periodicity and Point Defect Density along Dislocations*, Arizona State University, Peoria, AZ, USA **2002**.
- [34] B. Radisavljevic, A. Radenovic, J. Brivio, V. Giacometti, A. Kis, *Nat. Nanotechnol.* **2011**, *6*, 147.